https://doi.org/10.1016/j.cej.2020.126684

Mathematical modeling and numerical analysis of alkaline zinc-iron flow batteries for energy storage applications

Ziqi Chen[a], Wentao Yu[a], Yongfu Liu[a,b], Yikai Zeng[c], Qijiao He[d], Peng Tan[a*], Meng Ni[d,e*]

[a.] Department of Thermal Science and Energy Engineering, University of Science and Technology of China (USTC), Hefei 230026, Anhui, China.
[b.] Shanghai JINGYI Electrical Apparatus Factory Co., Ltd. Shanghai 201700, China.
[c.] Institute of Engineering Thermophysics and New Energy, School of Mechanical Engineering, Southwest Jiaotong University, Chengdu, Sichuan, China.
[d.] Department of Building and Real Estate, The Hong Kong Polytechnic University, Hung Hom, Kowloon, Hong Kong, China.
[e.] Environmental Energy Research Group, Research Institute for Sustainable Urban Development (RISUD), The Hong Kong Polytechnic University, Hung Hom, Kowloon, Hong Kong, China.
* Corresponding authors:
Email: pengtan@ustc.edu.cn (Peng Tan)
Email: meng.ni@polyu.edu.hk (Meng Ni)

Abstract: The alkaline zinc-iron flow battery is an emerging electrochemical energy storage technology with huge potential, while the theoretical investigations are still absent, limiting performance improvement. A transient and two-dimensional mathematical model of the charge/discharge behaviors of zinc-iron flow batteries is established. After validated by experimental data, numerical analysis is carried out focusing on the influences of electrolyte flow rate and electrode geometry towards the electrochemical performance. The results demonstrate that a high flow rate, high electrode thickness, and porosity are favorable for battery performance. Following this finding, the parameters of a zinc-iron flow battery are optimized by utilizing a high flow rate of 50 mL min^{-1}, an asymmetrical structure with a negative electrode of 7 mm and a positive electrode of 10 mm, and high porosity of 0.98. With the optimal flow rate and geometry, the electrolyte utilization, coulombic efficiency, and energy

efficiency attain 99.91%, 98.08%, and 91.07%, respectively, significantly higher than those of the un-optimized design. This work provides a comprehensive strategy allowing for the improvement of the practical design of zinc-iron flow batteries.

Keywords: Zinc-iron flow battery; Aqueous electrolyte; Numerical simulation; Design optimization

1. Introduction

Developing renewable energy like solar and wind energy requires inexpensive and stable electric devices to store energy, since solar and wind are fluctuating and intermittent [1,2]. Flow batteries, with their striking features of high safety and high efficiency, are of great promise for energy storage applications [3–5]. Moreover, Flow batteries have the advantage of being independently framed for energy and power [6]. Herein, enormous efforts have been made in the exploration and development of flow battery technologies [7–12]. Among various kinds of flow batteries, rechargeable zinc-based batteries with aqueous electrolytes are predominant owing to the inexpensive zinc, great chemical and physical stability, high safety, and environmental friendliness [13–19]. Since the 1970s, various zinc-based flow batteries like zinc-bromine, zinc-nickel, and zinc-iodine flow batteries have been proposed and developed [20]. However, commercialization is hindered by many issues. For example, zinc-bromine batteries are unfriendly to the environment owing to the diffusion of bromine [21], the performance of zinc-nickel flow batteries is limited by the relatively low kinetics of nickel redox couple [22–25], while zinc-iodine flow batteries suffer from relatively high prices [20].

On the contrary, owing to the remarkable characteristics of low prices, environmental-friendliness, and outstanding energy density, the zinc-iron flow battery appears to be a promising candidate for electricity-storage applications [20]. To this end, numerous works have been made on zinc-iron flow batteries. For example, Gong et al. reported a double-membrane triple-electrolyte designed zinc-iron battery which achieved an outstanding power density of 676 mW cm^{-2} with less than $100 per kWh system capital cost [26]. To suppress zinc dendrite, Yuan et al. presented a high-performance alkaline zinc-iron flow battery, which combined a polybenzimidazole (PBI) membrane with a three-dimensional porous carbon felt electrode. At 160 mA cm^{-2} the coulombic efficiency and energy efficiency were 99.5% and 82.8%, respectively [27]. Chang et al. developed an alkaline zinc-iron flow battery with a combination of an economically mixed matrix membrane and extremely alkali-resistant microporous hollow spheres, which run stably for 500 cycles with the coulombic efficiency and energy efficiency reaching 98.6% and 88.3% at 80 mA cm^{-2} [28]. To address hydrolysis and crossover issues, Li et al. proposed a neutral zinc-iron flow battery utilizing $FeCl_2/ZnBr_2$ species easy to dissolve, which achieved the energy efficiency of 86.66 % at 40 mA cm^{-2} and exhibited over 100 stable cycles [29]. To avoid corrosion, Xie et al. developed an acidic zinc-iron redox flow battery with the Ac^{-}/HAc buffer solution, which operated within a potential window of 0.5–2.0 V, achieving the electrolyte utilization of nearly 90% and the energy efficiency of 71.1% [30]. Such works have boosted the development of zinc-iron flow batteries, whereas this technology is still in the infancy stage and many issues remain to be solved. The chemical activity of zinc

makes it easy for hydrogen evolution reaction, especially in acid media. The plating-stripping process at the negative half-cell limits the areal capacity of zinc-iron flow batteries. The operating current density is relatively low, while high working current densities will aggravate zinc dendrite and further cause severe polarization [20]. In general, enormous efforts are required for zinc-iron flow batteries to enable the transition of the laboratory level into commercialization.

All the above-mentioned works focus on experimental investigations. Mathematical numerical modeling can be a more efficient and economic method for understanding the influences of design parameters and optimizing the design parameters for performance improvement. For example, Knehr al. presented a two-dimensional, transient, isothermal model of the vanadium redox flow battery (VRFB), from which the mean errors of the voltage after a single charge-discharge cycle and the capacity loss after 45 cycles were 1.83% and 4.2%, respectively [31]. Oh al. reported a three-dimensional, transient, non-isothermal VRFB model, which revealed crucial electrochemical and transport phenomena within the battery by means of multi-dimensional profiles of ionic and electronic potentials, species concentrations, and temperature patterns [32]. From these investigations, it is reasonable to expect that the numerical analysis of zinc-iron batteries can also facilitate the battery design and promote the commercialization. However, different from VRFBs in which only liquid-phase reactions occur on the electrode, the zinc-iron batteries include the dissolution and precipitate reactions of metallic zinc, which inevitably change the structure and surface area of the electrode, complexing the modeling process. Moreover, to the best

of our knowledge, neither the mathematical model nor the numerical analysis has been reported on zinc-iron batteries yet.

Herein, a transient two-dimensional model to descript the charge and discharge processes of a zinc-iron battery is established for the first time. After comparing with the experimental data, the impacts of different parameters on the battery operation are investigated, such as the electrolyte flow rate, electrode thickness, and electrode porosity. Further, the optimal design parameters are proposed for performance improvement. This work can facilitate the advancement of zinc-iron flow batteries for electricity storage applications, and the model can also be extended to other flow batteries with dissolution-deposition mechanisms for design optimization.

2. Model development

Fig. 1 illustrates the structure of an alkaline zinc-iron flow battery. The $Fe(CN)_6^{3-}/Fe(CN)_6^{4-}$ and $Zn(OH)_4^{2-}/Zn$ pairs are employed as the positive and negative redox couples, separately. The electrolytes with active materials are stored in tanks and cycled through pipes driven by pumps. Both half cells adopt porous carbon felt as the electrodes where the electrochemical reactions take place. A membrane is sandwiched by two electrodes, playing a significant role in transferring charge-balancing ions and preventing redox species from crossing over. During charge/discharge, the redox reactions take place simultaneously at both electrodes as follows:

Negative electrode:

$$Zn(OH)_4^{2-} + 2e^- \underset{\text{discharge}}{\overset{\text{charge}}{\rightleftharpoons}} Zn + 4OH^- \quad \text{(I)}$$

$$Zn(OH)_4^{2-} \rightarrow ZnO + 2OH^- + H_2O \quad \text{(II)}$$

Positive electrode:

$$Fe(CN)_6^{4-} \underset{\text{discharge}}{\overset{\text{charge}}{\rightleftharpoons}} Fe(CN)_6^{3-} + e^- \quad \text{(III)}$$

Specifically, in the negative electrode, multiple phases are present at the solid-liquid interface of the electrode due to the conversion between soluble $Zn(OH)_4^{2-}$ ions and metallic zinc. During charge, $Zn(OH)_4^{2-}$ ions obtain electrons and are reduced to zinc deposition. While during discharge, zinc is oxidized and dissolves, which may further become ZnO when reaching the saturation value [33]. As the applied concentration of $Zn(OH)_4^{2-}$ (0.5 M) in this work is lower than the solubility, the presence of solid ZnO is neglected (Reaction II) and only the electrochemical conversion (Reaction I) is considered. For the positive electrode, $Fe(CN)_6^{4-}$ is converted into $Fe(CN)_6^{3-}$ by oxidation during charge (Reaction III). The above reactions go in the opposite direction during discharge.

To simply the modeling, several assumptions are adopted in this work:

1. The battery is working under an isothermal condition.

2. The fluid is considered incompressible.

3. Physical properties of all domains are assumed to be isotropic and homogeneous.

4. Both hydrogen and oxygen evolution reactions are ignored.

5. In the case of species transport, dilute solution approximation is employed.

6. Variances in concentration, potential, and pressure along the width of the battery are neglected.

7. The volume change due to water carriage through the membrane is ignored.

2.1 Governing equations

The charge transferred between the electrolyte and the solid-state electrode domain obeys the conservation of charge:

$$\nabla \cdot \vec{j}_l^e + \nabla \cdot \vec{j}_s^e = 0 \tag{1}$$

where $\vec{j}_l^e$ and $\vec{j}_s^e$ represent the ionic and electronic current densities, separately:

$$\vec{j}_l^e = F \sum_i z_i \vec{N}_i^e \tag{2}$$

$$\vec{j}_s^e = \sigma_s^e \nabla \phi_s^e \tag{3}$$

where F is Faraday constant, z_i denotes the charge number, $\vec{N}_i^e$ denotes the solute species flux, which can be determined by the Nernst-Planck equation:

$$\vec{N}_i^e = -D_i^{eff} \nabla c_i^e - z_i u_i^e c_i^e F \nabla \phi_l^e + \vec{v}_g c_i^e \tag{4}$$

in which the mass transfer owing to diffusion, migration, and convection is presented. u_i^e is the ionic mobility, c_i^e is the species concentration in the bulk solution, ϕ_l^e and $\vec{v}_g$ are the potential and velocity of electrolyte, respectively. The effective diffusion coefficient D_i^{eff} is determined by the Bruggemann correlation:

$$D_i^{eff} = \varepsilon^{3/2} D_i \tag{5}$$

According to the dilute solution approximation, the ionic mobility u_i^e is given by the Nernst-Einstein equation:

$$u_i^e = \frac{D_i^{eff}}{RT} \tag{6}$$

in which R and T represent the universal gas constant and temperature, separately.

To descript the rates of electrochemical reactions, the Butler-Volmer equation is given for the positive (+) and negative (-) electrodes:

$$FD_{Fe^{2+}}\left(\frac{c_{Fe^{2+}}^e - c_{Fe^{2+}}^s}{r_p}\right) = Fk_+ (c_{Fe^{2+}}^e)^{(1-\alpha_+)} (c_{Fe^{3+}}^e)^{\alpha_+} \left[\left(\frac{c_{Fe^{2+}}^s}{c_{Fe^{2+}}^e}\right) \exp\left(\frac{(1-\alpha_+)F\eta_-}{RT}\right) - \left(\frac{c_{Fe^{3+}}^s}{c_{Fe^{3+}}^e}\right) \exp\left(\frac{-\alpha_+ F\eta_-}{RT}\right)\right] \tag{7a}$$

$$FD_{Fe^{3+}}\left(\frac{c^e_{Fe^{3+}}-c^s_{Fe^{3+}}}{r_p}\right)=Fk_+(c^e_{Fe^{2+}})^{(1-\alpha_+)}(c^e_{Fe^{3+}})^{\alpha_+}\left[\left(\frac{c^s_{Fe^{2+}}}{c^e_{Fe^{2+}}}\right)\exp\left(\frac{(1-\alpha_+)F\eta_-}{RT}\right)-\left(\frac{c^s_{Fe^{3+}}}{c^e_{Fe^{3+}}}\right)\exp\left(\frac{-\alpha_+F\eta_-}{RT}\right)\right] \quad (7b)$$

$$I_-=a_-Fk_-(c_{OH^-})^{(1-\alpha_-)}(c_{Zn(OH_4)^{2-}})^{\alpha_-}\left[\left(\frac{c_{OH^-}}{c_{OH^-,ref}}\right)^4\left(\frac{M_{Zn}}{M_{Zn,ref}}\right)\exp\left(\frac{2(1-\alpha_-)F\eta_-}{RT}\right)-\left(\frac{c_{Zn(OH_4)^{2-}}}{c_{Zn(OH_4)^{2-},ref}}\right)\exp\left(\frac{-2\alpha_-F\eta_-}{RT}\right)\right] \quad (7c)$$

where I represents the local reaction current density, a denotes the specific active surface area, k and α denote the standard rate constant and charge transfer coefficient, respectively. r_p represents the mean pore radius of the electrode, c_i^s represents the species concentration at the interface of liquid (electrolyte) and solid (electrode), $D_{Fe^{2+}}$ and $D_{Fe^{3+}}$ represent the diffusion coefficient of $Fe(CN)_6^{4-}$ and $Fe(CN)_6^{3-}$, separately. η denotes the overpotential and is determined by the following equation:

$$\eta_j=\phi_l^e-\phi_s^e-E_{0,j} \quad (8)$$

where $E_{0,j}$ is the equilibrium potential of each half-cell and can be determined from the Nernst equations:

$$E_{0,-}=E_{0,-}^{'}+\frac{RT}{F}\ln\left(\frac{c^e_{Fe^{3+}}}{c^e_{Fe^{2+}}}\right) \quad (9)$$

$$E_{0,+}=E_{0,+}^{'}+\frac{RT}{F}\ln\left(\frac{c^e_{Zn(OH_4)^{2-}}}{c^{e\,4}_{OH^-}}\right) \quad (10)$$

2.1.1 Mass conservation in the electrode

Each of the charged species in the porous regions is defined by the mass conservation shown below:

$$\frac{\partial}{\partial t}(\varepsilon c_i^e)+\nabla\cdot\vec{N}_i^e=-S_i \quad (11)$$

where ε denotes the electrode porosity, and S_i represents the source term.

For the negative electrode, the porosity changes owing to the zinc deposition during the charge process, which can be determined as:

$$\frac{\partial \varepsilon}{\partial t} = \frac{1}{2F}\frac{MW^{Zn}}{\rho^{Zn}} a\_I\_ \tag{12}$$

where MW and ρ denote the molecular weight and density, separately. The term on the right side demonstrates the electrode volume change due to the transformation of $Zn(OH_4)^{2-}$ to zinc.

The effective specific surface area of the negative electrode changes as a result of zinc deposition and can be described as follows [34]:

$$\frac{a}{a_0} = 1 - (\frac{\varepsilon_p}{\varepsilon})^p \tag{13}$$

where a_0 denotes the initial specific active surface area, ε_p denotes the volume fraction of the solid products, p denotes a geometric factor that illustrates the morphology of the deposition covering the electrode surface, and the value is chosen as a constant of 0.5 in this work.

2.1.2 Mass conservation in the membrane

Mass balance principle is applied to each of the charged species in the membrane region:

$$\frac{\partial c_i^m}{\partial t} = -\nabla \cdot \vec{N}_i^m \tag{14}$$

where c_i^m denotes the species concentration in the membrane, and $\vec{N}_i^m$ is calculated from the Nernst-Planck equation. Unlike the electrolyte in the porous electrode, electroneutrality is not applied to the solution in the membrane. Assuming that only water and protons are present in the membrane, and the proton concentration satisfies the following equation:

$$z_f c_f + c_{H^+} = 0 \tag{15}$$

where z_f and c_f represent the numbers and concentration of the fixed site charge in the ion-exchange membrane, respectively. The value of c_{H^+} is regarded as constant.

In the case of the membrane, the velocity $\overrightarrow{v}^m$ in the Nernst-Planck equation can be calculated from a different form of the Schlogl equation:

$$\overrightarrow{v}^m = -\frac{\kappa_p}{\mu_w}\nabla p - \frac{\kappa_\phi}{\mu_w} c_f F(\nabla \phi_l^m + \nabla \phi_{diff}^m) \tag{16}$$

where μ_w represents the viscosity of water, κ_ϕ and κ_p denote the electro-kinetic and the hydraulic permeability, respectively. The first term on the right side illustrates the osmosis of water through the membrane caused by the different pressure between the two half-cells. The last term signifies that the fluid and the charged species have viscous interactions resulting in the electro-osmotic convection, where $F(\nabla \phi_l^m + \nabla \phi_{diff}^m)$ represents the body force acting on the mobile ions. The term $\nabla \phi_l^m$ is the potential difference of liquid in the membrane region, $\nabla \phi_{diff}^m$ denotes the effective diffusion potential illustrating the viscous resistance caused by ion diffusion and can be defined as:

$$\nabla \phi_{diff}^m = \frac{F \sum z_i D_i^m c_i^m}{\sigma_{eff}^m} \tag{17}$$

where σ_{eff}^m denotes the membrane effective conductivity:

$$\sigma_{eff}^m = \frac{F^2}{RT} \sum_i z_i^2 D_i^m c_i^m \tag{18}$$

2.2 Boundary conditions

At the interface of electrode and current collector, along the top and bottom of the membrane, the fluxes of the species are supposed as zero:

$$0 = \begin{cases} -\mathrm{n} \cdot \vec{N}_i^e & x = x_1 \; and \; x = x_4 \\ -\mathrm{n} \cdot \vec{N}_i^m & y = 0 \; and \; y = h_{cell} \end{cases} \tag{19}$$

At the bottom entrances of the electrodes, the electrolyte velocity and species concentrations are used to calculate the inward fluxes of the species:

$$y = 0(inlet) \begin{cases} -\mathrm{n} \cdot \vec{v} = \frac{\omega}{\varepsilon w_{cell} L_e} \\ c_i^e = c_i^{in}(t) \end{cases} \quad (20)$$

where w_{cell} is the width of the cell, L_e is the electrode thickness, and ω denotes the volumetric flow rate. At the top exits of electrodes, the pressure can be taken as constant, and species flux driven by diffusion is supposed as zero:

$$y = h_{cell}(outlet) \begin{cases} P = P_{out} \\ -\vec{n} \cdot D_i^{eff} \nabla c_i^e = 0 \end{cases} \quad (21)$$

A Neumann condition is applied to all boundaries of the pressure equation integral domain, in addition to the entrances and exits:

$$\vec{n} \cdot \nabla P = 0 \quad (22)$$

The current density is set as constant, and at the current collectors the boundary conditions during charge are given as follows:

$$-\vec{n} \cdot \vec{j}_s^{cc} = \begin{cases} -\frac{I_{app}}{h_{cell} w_{cell}} & x = 0 \\ \frac{I_{app}}{h_{cell} w_{cell}} & x = x_5 \end{cases} \quad (23)$$

the term I_{app} denotes the applied current density, of which the signs are opposite when charging and discharging. Thus, at the top and bottom of the electrodes and membrane, an electrical insulation condition is applied:

$$-\vec{n} \cdot \vec{j}_s^{cc} = -\vec{n} \cdot \vec{j}_s^{e} = -\vec{n} \cdot \vec{j}_l^{m} = -\vec{n} \cdot \vec{j}_l^{e} = 0 \;\; y = 0 \; and \; y = h_{cell} \quad (24)$$

The boundary condition at the negative ('−') current collector is to be grounded:

$$\phi_s^{cc} = 0 \;\; x = 0 \quad (25)$$

During the operation, the species concentrations and the volumes of the electrolytes are changing all the time as a result of the redox reactions and species crossover. To illustrate the species concentration changes, the conservation of mass is used to simulate the inlet concentration for each species :

$$\frac{V}{h_{cell}}\frac{d}{dt}\left(c_i^{in}\right) = \int_{outlet}(\vec{N}_i \cdot \vec{n})\,dS - \int_{inlet}\left(\vec{N}_i \cdot \vec{n}\right)dS \quad c_i^{in}(0) = c_i^0 \tag{26}$$

in which V represents the total volume of the electrolyte flowing through the tank. $\vec{N}_i \cdot \vec{n}$ denotes the molar fluxes of the respective electrolyte species in the normal direction to the boundary.

3. Numerical results

3.1 Calculation details

To compare with the experimental results, the initial parameters such as the geometric sizes are adopted from literature, as listed in **Table 1**. The kinetics values and general parameters applied in calculations are given in **Table 2** and **Table 3**, separately.

The model was solved via a finite-element method using COMSOL Multiphysics software with the modules of the tertiary current distribution and ODE options. The mesh includes 2556 elements, and the relative tolerance of 10^{-3} was utilized. The cut-off voltages of the charge and discharge processes were 1.94 V and 1.50 V, respectively.

3.2 Model validation

The performance predictions of the present model were compared with experimental data from Yuan's work using the same parameters at the current density of 60 mA cm^{-2} [27]. As displayed in **Fig. 2**, a good agreement in voltages is observed with the maximum variation of 2.45% (Table S1), illustrating that the present model is able to simulate the discharge-charge behavior of a zinc-iron flow battery. The slight discrepancies between the voltage profiles may come from the lack of accurate data (e.g., transfer coefficient) and the neglect of side reactions such as hydrogen evolution.

The zinc deposition may cause the blockage of electrode pores and lead to severe polarization when charge ends, which can hardly be simulated perfectly. Moreover, the crossover of active materials can also cause capacity loss, which is neglected in the simulation.

Fig. 3 depicts the species concentration distribution of the battery at 50% state of charge or discharge. The simulation results indicate different distribution behaviors between positive and negative electrodes. During charge, from **Fig. 3a**, the concentration near the current collector appears to be higher, which can be attributed to the different conductivity of the electrode (the electronic conductor) and the electrolyte (the ionic conductor). Since the electrolyte flow direction is from bottom to top, there is no enough time for $Zn(OH)_4^{2-}$ ions to consume completely at the entrance, leading the concentration at the bottom much higher than that at the top. During discharge, as shown in **Fig. 3b**, a similar trend is exhibited but with more uniform distribution, which is due to the resolution of the zinc raising the porosity, resulting in better transport of species. Thus, the flow condition and the electrode structure are crucial to the battery performance, and their influences are thus detailedly investigated in the following sections.

4. Analysis and discussion

In this section, relying on the developed model of the zinc-iron flow battery, the influences of the applied flow rate and electrode geometry are investigated. From the analysis, the optimal performance with well-design parameters is also presented.

4.1 Effects of flow rate

To reveal the effects of flow rate, the charge and discharge voltage profiles of the zinc-iron flow battery with three different volumetric flow rates are demonstrated in **Fig. 4**. It appears that the charge voltage decreases and a larger capacity is acquired when the flow rate gets higher. During discharge, with the flow rate rising, both capacity and voltage increase. The battery performance is summarized in **Table 4**. At a small volumetric flow rate of 10 mL min^{-1}, the electrolyte utilization only researches 80.13%, and the coulombic efficiency and energy efficiency are 92.98% and 86.82%, separately. As the volumetric flow rate increases to 50 mL min^{-1}, the electrolyte utilization improves to 93.76%, and the coulombic efficiency and energy efficiency reach 98.82% and 92.60%, respectively. Thus, a higher flow rate is expected to be more favorable for high performance.

To look inside the reason for the performance improvement at a higher flow rate, the species distribution at 50% charge and discharge stages are shown in **Fig. 5a** and **5b**, respectively. The uniformity of species concentration distribution increases with a growth of the flow rate during both charge and discharge. As shown in Table S2, the standard deviation and the coefficient of variation of the species concentration are the least at the flow rate of 50 mL min^{-1}. According to this result, the electrolyte is efficiently circulated at higher flow rates, which promotes the active species transport, thereby, reducing the concentration overpotential. When adopting a larger flow rate, the performance will keep improving, but the enhancement is limited. For example, the electrolyte utilization and energy efficiency become 93.93% and 94.83%, respectively, at a very high rate of 300 mL min^{-1}. It is worth noting that here we only consider the

effects of flow rate on the battery performance, while a higher flow rate may require more pump work. Hence, the net obtained energy should be carefully estimated in practical applications.

4.2 Effects of electrode geometry

4.2.1 Electrode thickness

Besides the operating conditions, the electrode geometry also plays a significant role in the charge/discharge performance. **Fig. 6** shows the simulated charge and discharge voltage profiles of the zinc-iron flow battery with different electrode thicknesses at the same volumetric flow rate of 15 mL min^{-1}. Upon charging, both the porosity and the specific surface area decrease as a result of zinc deposition (Fig. S1), the behavior during discharge is the opposite as zinc dissolve (Fig. S2). As the electrode thickness is increased from 5 mm to 10 mm, the voltage drop can be observed. At the end of charge, the porosity and the specific surface area of the electrode with the thickness of 10 mm are the greatest, demonstrating the fact that the enlarged charge transport pathway in the thicker electrode leads to better electrolyte utilization. During discharge, with the electrode thickness increasing, the capacity improves remarkably while the voltage reduces a little. This may be because that with a growth of the thickness, the ohmic loss increases owing to the longer routes for electron and ion transport. While a thicker electrode offers more surface areas, and thus improving the utilization of the electrolyte and leading to a higher discharge capacity.

To explicate the intrinsic mechanism of the electrode thickness on the battery performance, the concentration distribution in both electrodes at the 50% SOC during

charge and discharge is examined, as displayed in **Fig. 7**. From **Fig. 7a**, the concentration in the negative electrode (left side) is more evenly distributed at a small electrode thickness, while an opposite pattern is shown at the positive electrode (right side). This can be explained by that the average concentration increases with an increase of the electrode thickness owing to the incomplete depletion of $Zn(OH)_4^{2-}$ at the negative electrode (Table S3). As for the positive electrode during charge, the average concentration and the standard deviation of the 10 mm electrode is the lowest, indicating that as the electrode getting thicker, the $Fe(CN)_6^{4-}$ ions are insufficiently utilized. However, the voltage profile shows the opposite trend, which might because the activation overpotential is the dominating mechanism that a thicker electrode has a larger reaction surface area, compensating the concentration polarization. During discharge, the concentration of the electrode with a thickness of 5 mm is the most uniform. This is because the diffusion distances of ions at the thinner electrode are short, making it easier to transport and react sufficiently. From the results in **Table 5**, the electrolyte utilization, coulombic efficiency, and energy efficiency increase as the electrode thickness increases, which can be explained by the fact that the potential loss is compromised by the capacity increase when the electrode gets thicker.

4.2.1 Electrode porosity

Fig. 8 compares the charge and discharge voltage profiles of the cell with different electrode porosity and the electrode thickness of 7 mm at the flow rate of 15 mL min^{-1}. When charging, a lower voltage at the higher porosity is observed. During discharge, the voltage and capacity increase a lot with the increase of porosity. As displayed in

Fig. 9, during both charge and discharge, the concentration is more uniform at higher porosity (Table S4), which is due to the fact that the ion transport pathway is enlarged, decreasing the internal resistance. In addition, high porosity means a larger specific surface area for electrochemical reactions, promoting the contact among the active species in the porous electrode, resulting in the sufficient utilization of the electrolyte. Consequently, the overpotential is the lowest for the battery with the porosity of 0.94, and the battery owns the best performance, as summarized in **Table 6**. Nevertheless, with the porosity increasing, the mechanical strength of the carbon felt electrode will decrease simultaneously, which is hard to simulate but should be noticed in the actual operation.

4.3 Parameter design for performance improvement

According to the analysis presented above, a high flow rate and a high porosity are beneficial to the zinc-iron flow battery, while the concentration distribution patterns are different at the negative and positive electrodes. Thereby, to investigate the role of electrode thickness playing in the optimization, we compared the performance of the battery with the electrode thicknesses of both 7 mm, 10 mm, and asymmetry designs of the mixed thickness at a porosity of 0.98 and a volumetric flow rate of 50 mL min^{-1}. As the results shown in Table S5, the coulombic efficiency and energy efficiency of the battery utilizing the negative electrode of 7 mm and the positive electrode of 10 mm is the highest, indicating that the asymmetry design is as favorable as expected when the positive electrode being thicker than the negative electrode. Therefore, the asymmetrical electrode with 7 mm in the negative electrode and 10 mm in the positive

electrode is applied in the optimization with high porosity and flow rate. **Fig. 10a** shows that a much larger capacity is obtained when utilizing the optimized parameters, and the charge voltage is reduced on charging. The comparisons of concentration distribution between the optimization and original designs are shown in **Fig. 10b** and **10c**. The species of the battery adopting modified parameters distribute much more uniform, confirming that the applied parameters are favorable to the optimization of the zinc-iron flow batteries. As presented in **Table 7**, the optimized battery exhibits high coulombic efficiency (CE=99.18%) and outstanding energy efficiency (EE=92.84%) comparing to the initial design, demonstrating an impressive performance enhancement.

5. Conclusions

In this work, a two-dimensional, transient, and isothermal mathematical model for an alkaline zinc-iron flow battery has been developed for the first time. The comparison of the simulation results with experimental data demonstrates that the model can accurately capture the charge and discharge behaviors of the battery. Based on this model, the in-depth analysis of key parameters is carried out, including the electrolyte flow rate, the electrode thickness, and the electrode porosity. The results demonstrate that a high flow rate can promote active species transport and reduce the concentration overpotential, leading to high electrolyte utilization. As the electrode thickness increasing, the capacity improves remarkably owing to the increased surface areas, while the discharge voltage reduces a little due to the longer routes for electron and ion transport. As the potential loss can be compromised by the capacity enhancement, the

energy efficiency increases as an increase of the electrode thickness. With an increase of porosity, the ion transport pathway is enlarged and the specific surface area is enlarged for electrochemical reactions, resulting in high energy density and efficiency. Inspired by the numerical analysis, the parameters of a zinc-iron flow battery have been optimized by utilizing a high flow rate of 50 mL min^{-1}, an asymmetrical thickness of 7 mm in the negative electrode and 10 mm in the positive electrode, and high porosity of 0.98, by which the electrolyte utilization, coulombic efficiency, and energy efficiency attain 98.62%, 99.18%, and 92.84%, respectively, significantly higher than those of the initial design. This work can favor the development of high-performance zinc-iron flow batteries and be extended to other flow batteries for design optimization.

Declaration of interests

The authors declare no competing interests.

CRediT authorship contribution statement

Ziqi Chen: Conceptualization, Investigation, Methodology, Writing - original draft. **Wentao Yu**: Investigation, Methodology. **Yongfu Liu**: Investigation. **Yikai Zeng**: Writing - review & editing, Funding acquisition. **Qijiao He**: Writing-review & editing. **Peng Tan**: Supervision, Project administration, Funding acquisition, Writing - review & editing. **Meng Ni**: Supervision, Funding acquisition, Writing - review & editing.

Acknowledgments

P. Tan thanks the funding support from CAS Pioneer Hundred Talents Program (KJ2090130001), Shanghai JINGYI Electrical Apparatus Factory Co., Ltd. (ES2090130106), USTC Research Funds of the Double First-Class Initiative

(YD2090002006), and USTC Tang Scholar. Y.K. Zeng thanks the funding support from National Natural Science Foundation of China (No. 51806182). M. Ni thanks the funding support from The Hong Kong Polytechnic University (G-YW2D) and a grant (Project Number: PolyU 152214/17E and PolyU 152064/18E) from Research Grant Council, University Grants Committee, Hong Kong SAR.

Nomenclature

a	specific electroactive area ($m^2\ m^{-3}$)
c	concentration (mol m^{-3})
D	diffusion coefficient ($m^2\ s^{-1}$)
E_0	equilibrium potential (V)
E_0'	standard reaction potential (V)
F	Faraday constant (96,485 C mol^{-1})
h	height
I	current density (A m^{-2})
k	reaction rate
L	component thickness (m)
n	transferred electron
$\vec{n}$	outward normal vector
$\vec{N}$	molar species flux (mol $m^{-2}\ s^{-1}$)
P	pressure
p	geometric factor
R	universal gas constant (8.314 J $mol^{-1}\ K^{-1}$)
S	source (mol $m^{-3}\ s^{-1}$)
T	temperature (K)
t	time
u	ion mobility
V	volume (mL)
$\vec{v}$	velocity (m s^{-1})
w	component width (m)
x	distance along cell width (m)
y	distance along cell height (m)
z	valence

Greek

α	transfer coefficient
η	overpotential (V)
ε	porosity
ε_p	volume fraction of solid
κ	permeability (m^2)
ρ	density (kg m^{-3})
σ	conductivity (S m^{-1})
μ_w	dynamic viscosity of water
ω	volumetric flow rate (m^3 s^{-1})
ϕ	electric potential (V)

Subscripts

cell	property of cell
cha	charge
dis	discharge
diff	diffusion
D	pertinent to diffusion
e	electrolyte phase
eff	effective, corrected for tortuosity
f	fixed membrane structure
g	electrolyte
l	liquid or ionic
j	reaction
ref	reference
s	solid or electronic
i	specie
+	positive half-cell
−	negative half-cell

Superscripts

e	electrode or electrolyte domain
eff	effective value
m	membrane domain
out	outlet
s	surface

References

[1] M. Song, H. Tan, D. Chao, H.J. Fan, Recent Advances in Zn-Ion Batteries, Advanced Functional Materials. 28 (2018) 1–27. https://doi.org/10.1002/adfm.201802564.

[2] W. Xu, Y. Wang, Recent Progress on Zinc-Ion Rechargeable Batteries, Nano-Micro Letters. 11 (2019) 1–30. https://doi.org/10.1007/s40820-019-0322-9.

[3] Z. Yuan, H. Zhang, X. Li, Ion conducting membranes for aqueous flow battery

systems, Chemical Communications. 54 (2018) 7570–7588. https://doi.org/10.1039/C8CC03058H.
[4] C. Zhang, L. Zhang, Y. Ding, X. Guo, G. Yu, Eutectic Electrolytes for High-Energy-Density Redox Flow Batteries, ACS Energy Letters. 3 (2018) 2875–2883. https://doi.org/10.1021/acsenergylett.8b01899.
[5] G.L. Soloveichik, Flow Batteries: Current Status and Trends, Chemical Reviews. 115 (2015) 11533–11558. https://doi.org/10.1021/cr500720t.
[6] L. Li, S. Kim, W. Wang, M. Vijayakumar, Z. Nie, B. Chen, J. Zhang, G. Xia, J. Hu, G. Graff, J. Liu, Z. Yang, A stable vanadium redox-flow battery with high energy density for large-scale energy storage, Advanced Energy Materials. 1 (2011) 394–400. https://doi.org/10.1002/aenm.201100008.
[7] W. Lu, C. Xie, H. Zhang, X. Li, Inhibition of Zinc Dendrite Growth in Zinc-Based Batteries, ChemSusChem. 11 (2018) 3996–4006. https://doi.org/10.1002/cssc.201801657.
[8] R. Imhof, N. Petr, Technical papers electrochemical science and technology, October. 145 (1998) 3313–3319. https://doi.org/10.1149/1.1838201.
[9] A. Khor, P. Leung, M.R. Mohamed, C. Flox, Q. Xu, L. An, R.G.A. Wills, J.R. Morante, A.A. Shah, Review of zinc-based hybrid flow batteries: From fundamentals to applications, Materials Today Energy. 8 (2018) 80–108. https://doi.org/10.1016/j.mtener.2017.12.012.
[10] J. McBreen, Rechargeable zinc batteries, Journal of Electroanalytical Chemistry. 168 (1984) 415–432. https://doi.org/10.1016/0368-1874(84)87113-0.
[11] X.L. Zhou, T.S. Zhao, L. An, Y.K. Zeng, L. Wei, Modeling of ion transport through a porous separator in vanadium redox flow batteries, Journal of Power Sources. 327 (2016) 67-76. https://doi.org/10.1016/j.jpowsour.2016.07.046.
[12] G. Fang, J. Zhou, A. Pan, S. Liang, Recent Advances in Aqueous Zinc-Ion Batteries, ACS Energy Letters. 3 (2018) 2480–2501. https://doi.org/10.1021/acsenergylett.8b01426.
[13] Y. Zeng, Z. Yang, F. Lu, Y. Xie, A novel tin-bromine redox flow battery for large-scale energy storage, Applied Energy. 255 (2019) 113756. https://doi.org/10.1016/j.apenergy.2019.113756.
[14] Y. Li, J. Fu, C. Zhong, T. Wu, Z. Chen, W. Hu, K. Amine, J. Lu, Batteries: Recent Advances in Flexible Zinc-Based Rechargeable Batteries, Advanced Energy Materials. 9 (2019) 1970001. https://doi.org/10.1002/aenm.201970001.
[15] J. Ming, J. Guo, C. Xia, W. Wang, H.N. Alshareef, Zinc-ion batteries: Materials, mechanisms, and applications, Materials Science and Engineering R: Reports. 135 (2019) 58-84. https://doi.org/10.1016/j.mser.2018.10.002.
[16] C. Xu, B. Li, H. Du, F. Kang, Energetic zinc ion chemistry: The rechargeable zinc ion battery, Angewandte Chemie International Edition. 51 (2012) 933–935. https://doi.org/10.1002/anie.201106307.
[17] B. Lee, H.R. Lee, H. Kim, K.Y. Chung, B.W. Cho, S.H. Oh, Elucidating the intercalation mechanism of zinc ions into α-MnO_2 for rechargeable zinc batteries, Chemical Communications. 51 (2015) 9265–9268. https://doi.org/10.1039/c5cc02585k.

[18] Q. Yang, F. Mo, Z. Liu, L. Ma, X. Li, D. Fang, S. Chen, S. Zhang, C. Zhi, Activating C-Coordinated Iron of Iron Hexacyanoferrate for Zn Hybrid-Ion Batteries with 10000-Cycle Lifespan and Superior Rate Capability, Advanced Materials. 31 (2019) 1–9. https://doi.org/10.1002/adma.201901521.
[19] W. Xu, K. Zhao, W. Huo, Y. Wang, G. Yao, X. Gu, H. Cheng, L. Mai, C. Hu, X. Wang, Diethyl ether as self-healing electrolyte additive enabled long-life rechargeable aqueous zinc ion batteries, Nano Energy. 62 (2019) 275–281. https://doi.org/10.1016/j.nanoen.2019.05.042.
[20] Z. Yuan, Y. Yin, C. Xie, H. Zhang, Y. Yao, X. Li, Advanced Materials for Zinc-Based Flow Battery: Development and Challenge, Advanced Materials. 31 (2019) 1–27. https://doi.org/10.1002/adma.201902025.
[21] J.H. Yang, H.S. Yang, H.W. Ra, J. Shim, J.D. Jeon, Effect of a surface active agent on performance of zinc/bromine redox flow batteries: Improvement in current efficiency and system stability, Journal of Power Sources. 275 (2015) 294–297. https://doi.org/10.1016/j.jpowsour.2014.10.208.
[22] Y. Cheng, H. Zhang, Q. Lai, X. Li, D. Shi, Performance gains in single flow zinc-nickel batteries through novel cell configuration, Electrochimica Acta. 105 (2013) 618–621. https://doi.org/10.1016/j.electacta.2013.05.024.
[23] Y.F. Yuan, X.H. Xia, J.B. Wu, J.L. Yang, Y.B. Chen, S.Y. Guo, Nickel foam-supported porous $Ni(OH)_2$/NiOOH composite film as advanced pseudocapacitor material, Electrochimica Acta. 56 (2011) 2627–2632. https://doi.org/10.1016/j.electacta.2010.12.001.
[24] S. Klaus, Y. Cai, M.W. Louie, L. Trotochaud, A.T. Bell, Effects of Fe electrolyte impurities on $Ni(OH)_2$/NiOOH structure and oxygen evolution activity, Journal of Physical Chemistry C. 119 (2015) 7243–7254. https://doi.org/10.1021/acs.jpcc.5b00105.
[25] C.-C. Hu, K.-H. Chang, T.-Y. Hsu, The Synergistic Influences of OH^- Concentration and Electrolyte Conductivity on the Redox Behavior of $Ni(OH)_2$/NiOOH, Journal of The Electrochemical Society. 155 (2008) F196. https://doi.org/10.1149/1.2945911.
[26] K. Gong, X. Ma, K.M. Conforti, K.J. Kuttler, J.B. Grunewald, K.L. Yeager, M.Z. Bazant, S. Gu, Y. Yan, A zinc-iron redox-flow battery under $100 per kW h of system capital cost, Energy and Environmental Science. 8 (2015) 2941–2945. https://doi.org/10.1039/c5ee02315g.
[27] Z. Yuan, Y. Duan, T. Liu, H. Zhang, X. Li, Toward a Low-Cost Alkaline Zinc-Iron Flow Battery with a Polybenzimidazole Custom Membrane for Stationary Energy Storage, iScience. 3 (2018) 40–49. https://doi.org/10.1016/j.isci.2018.04.006.
[28] N. Chang, Y. Yin, M. Yue, Z. Yuan, H. Zhang, Q. Lai, X. Li, A Cost-Effective Mixed Matrix Polyethylene Porous Membrane for Long-Cycle High Power Density Alkaline Zinc-Based Flow Batteries, Advanced Functional Materials. 29 (2019) 1–11. https://doi.org/10.1002/adfm.201901674.
[29] C. Xie, Y. Duan, W. Xu, H. Zhang, X. Li, A Low-Cost Neutral Zinc–Iron Flow Battery with High Energy Density for Stationary Energy Storage, Angewandte Chemie International Edition. 56 (2017) 14953–14957.

https://doi.org/10.1002/anie.201708664.
[30] Z. Xie, Q. Su, A. Shi, B. Yang, B. Liu, J. Chen, X. Zhou, D. Cai, L. Yang, High performance of zinc-ferrum redox flow battery with Ac^-/HAc buffer solution, Journal of Energy Chemistry. 25 (2016) 495–499. https://doi.org/10.1016/j.jechem.2016.02.009.
[31] K.W. Knehr, E. Agar, C.R. Dennison, A.R. Kalidindi, E.C. Kumbur, A transient vanadium flow battery model incorporating vanadium crossover and water transport through the membrane, Journal of the Electrochemical Society. 159 (2012) 1446–1459. https://doi.org/10.1149/2.017209jes.
[32] K. Oh, H. Yoo, J. Ko, S. Won, H. Ju, Three-dimensional, transient, nonisothermal model of all-vanadium redox flow batteries, Energy. 81 (2015) 3-14. https://doi.org/10.1016/j.energy.2014.05.020.
[33] H. G. Dietrich and J. Johnston, Equilibrium between crystalline zinc hydroxide and aqueous solutions of ammonium hydroxide and of sodium hydroxide, Journal of the American Chemical Society. 49 (1927) 1419-1431. https://doi.org/10.1021/ja01405a005
[34] P. Tan, H.R. Jiang, X.B. Zhu, L. An, C.Y. Jung, M.C. Wu, L. Shi, W. Shyy, T.S. Zhao, Advances and challenges in lithium-air batteries, Applied Energy. 204 (2017) 780–806. https://doi.org/10.1016/j.apenergy.2017.07.054.
[35] D. P, CRC Handbook of Chemistry and Physics, Journal of Molecular Structure. (1992). https://doi.org/10.1016/0022-2860(92)85083-s.

Table captions

Table 1 Parameters used in the simulation

Table 2 Kinetic parameters used in the simulation

Table 3 General parameters

Table 4 Battery performance at different flow rates

Table 5 Battery performance with different electrode thicknesses

Table 6 Battery performance with different electrode porosity

Table 7 Comparison of the battery performance under initial and optimization designs

Table 1 Parameters used in the simulation

Parameter	Symbol	Value	Unit	Ref.
Geometrical properties				
Thickness of the membrane	L_m	3.5×10^{-5}	m	[27]
Thickness of the electrode	L_e	0.01	m	
Porosity of the electrode	ε	0.94	-	[27]
Specific surface area of the electrode	a	5.0×10^{4}	m^{-1}	
Height of the cell	h_{cell}	0.06	m	[27]
Width of the cell	w_{cell}	0.08	m	[27]
Electrolyte properties				
Diffusion coefficient of OH^-	$D_{\mathrm{OH-}}$	5.27×10^{-9}	$m^2\ s^{-1}$	[35]
Diffusion coefficient of K^+	$D_{\mathrm{K+}}$	1.96×10^{-9}	$m^2\ s^{-1}$	[35]
Diffusion coefficient of Na^+	$D_{\mathrm{Na+}}$	1.33×10^{-9}	$m^2\ s^{-1}$	[35]
Diffusion coefficient of $Zn(OH)_4^{2-}$	$D_{\mathrm{Zn(OH)_4^{2-}}}$	3.10×10^{-10}	$m^2\ s^{-1}$	[35]
Diffusion coefficient of $Fe(CN)_6^{4-}$	$D_{\mathrm{Fe(CN)_6^{4-}}}$	7.35×10^{-10}	$m^2\ s^{-1}$	[35]
Diffusion coefficient of $Fe(CN)_6^{3-}$	$D_{\mathrm{Fe(CN)_6^{3-}}}$	8.96×10^{-10}	$m^2\ s^{-1}$	[35]
OH^- initial concentration in negative electrolyte	$c^0_{-,\mathrm{OH-}}$	4000	$mol\ m^{-3}$	[27]
OH^- initial concentration in postive electrolyte	$c^0_{+,\mathrm{OH-}}$	3000	$mol\ m^{-3}$	[27]
$Zn(OH)_4^{2-}$ initial concentration in negative electrolyte	$c^0_{\mathrm{Zn(OH)_4^{2-}}}$	500	$mol\ m^{-3}$	[27]
Zn initial concentration in negative electrolyte	c^0_{Zn}	20	$mol\ m^{-3}$	[27]
Na^+ initial concentration in negative electrolyte	$c^0_{-,\mathrm{Na+}}$	4000	$mol\ m^{-3}$	[27]
Na^+ initial concentration in postive electrolyte	$c^0_{+,\mathrm{Na+}}$	1000	$mol\ m^{-3}$	[27]
$Fe(CN)_6^{4-}$ initial concentration	$c^0_{\mathrm{Fe(CN)_6^{4-}}}$	1000	$mol\ m^{-3}$	[27]

in postive electrolyte				
$Fe(CN)_6^{3-}$ initial concentration in postive electrolyte	$c^0_{Fe(CN)_6^{3-}}$	20	mol m^{-3}	[27]
K^+ initial concentration in postive electrolyte	c^0_{K+}	3000	mol m^{-3}	[27]

Table 2 Kinetic parameters used in the simulation

Parameter	Symbol	Value	Unit
Anodic transfer coefficients of negative reaction, charge	$\alpha^{a}_{-,cha}$	0.6	-
Cathodic transfer coefficients of negative reaction, charge	$\alpha^{c}_{-,cha}$	0.4	-
Anodic transfer coefficients of positive reaction, charge	$\alpha^{a}_{+,cha}$	0.6	-
Cathodic transfer coefficients of positive reaction, charge	$\alpha^{c}_{+,cha}$	0.4	-
Anodic transfer coefficients of negative reaction, discharge	$\alpha^{a}_{-,dis}$	0.5	-
Cathodic transfer coefficients of negative reaction, discharge	$\alpha^{c}_{-,dis}$	0.5	-
Anodic transfer coefficients of positive reaction, discharge	$\alpha^{a}_{+,dis}$	0.2	-
Cathodic transfer coefficients of positive reaction, discharge	$\alpha^{c}_{+,dis}$	0.8	-
Standard rate constant of negative reaction, charge	$k_{-,cha}$	4×10^{-8}	m s^{-1}
Standard rate constant of positive reaction, charge	$k_{+,cha}$	4×10^{-8}	m s^{-1}
Standard rate constant of negative reaction, discharge	$k_{-,dis}$	1×10^{-7}	m s^{-1}
Standard rate constant of positive reaction, discharge	$k_{+,dis}$	6×10^{-5}	m s^{-1}

Table 3 General parameters

Parameter	Symbol	Value	Unit	Ref.
General parameter				
Density of Zn	ρ_{Zn}	7,140	kg m^{-3}	
Molecular weight of Zn	MW_{Zn}	65.38	g mol^{-1}	
Operating temperature	T	298.15	K	
Conductivity of the electrode	σ	300	S m^{-1}	
Number of transferred electrons of negative reaction	n_-	2	-	
Number of transferred electrons of positive reaction	n_+	1	-	
Standard potential of negative reaction	$E'_{0,-}$	-1.41	V	[27]
Standard potential of positive reaction	$E'_{0,+}$	0.33	V	[27]
Electrolyte volume per half-cell	V	60	mL	[27]

Table 4 Battery performance at different flow rates

Volumetric flow rate (mL min^{-1})	Charge capacity (Ah L^{-1})	Discharge capacity (Ah L^{-1})	Electrolyte utilization (%)	Coulombic efficiency (%)	Charge energy (Wh L^{-1})	Discharge energy (Wh L^{-1})	Energy efficiency (%)
10	23.10	21.48	80.13	92.98	42.96	37.29	86.82
15	24.00	22.92	85.53	95.52	44.57	39.84	89.40
50	25.43	25.13	93.76	98.82	47.14	43.65	92.60

Table 5 Battery performance with different electrode thicknesses

Electrode thickness (mm)	Charge capacity (Ah L^{-1})	Discharge capacity (Ah L^{-1})	Electrolyte utilization (%)	Coulombic efficiency (%)	Charge energy (Wh L^{-1})	Discharge energy (Wh L^{-1})	Energy efficiency (%)
5	21.45	18.05	67.35	84.16	39.88	31.45	78.85
7	24.05	21.02	78.42	87.39	44.67	36.37	81.43
10	26.65	23.99	89.51	90.01	49.50	41.04	82.92

Table 6 Battery performance with different electrode porosity

Porosity	Charge capacity (Ah L^{-1})	Discharge capacity (Ah L^{-1})	Electrolyte utilization (%)	Coulombic efficiency (%)	Charge energy (Wh L^{-1})	Discharge energy (Wh L^{-1})	Energy efficiency (%)
0.70	20.80	17.72	66.11	85.19	38.80	30.30	78.11
0.80	22.75	19.68	73.42	86.50	42.38	33.90	79.98
0.94	24.00	22.92	85.53	95.52	44.57	39.84	89.40

Table 7 Comparison of the battery performance under initial and optimization designs

Design	Porosity	Electrode thickness (mm)	Volumetric flow rate (mL min^{-1})	Charge capacity (Ah L^{-1})	Discharge capacity (Ah L^{-1})	Electrolyte utilization (%)	Coulombic efficiency (%)	Charge energy (Wh L^{-1})	Discharge energy (Wh L^{-1})	Energy efficiency (%)
Initial	0.94	7	15	26.00	22.92	85.53	88.16	48.45	39.84	82.23
Optimization	0.98	7/10	50	26.65	26.43	98.62	99.18	49.20	45.68	92.84

Figure captions

Fig. 1 Scheme of a zinc-iron flow battery. The computational domain is from 0 to x_6.

Fig. 2 Comparison of the simulated voltage profiles of a zinc-iron flow battery at the current density of 60 mA cm^{-2} with the experimental data.

Fig. 3 The species distribution at 50% stage: (a) $Zn(OH)_4^{2-}$ (left side) and $Fe(CN)_6^{3-}$ (right side) during charge and (b) $Zn(OH)_4^{2-}$ (left side) and $Fe(CN)_6^{4-}$ (right side) during discharge.

Fig. 4 Charge and discharge voltage profiles of the battery at different flow rates.

Fig. 5 The species distribution at different flow rates at 50% stage: (a) $Zn(OH)_4^{2-}$ (left side) and $Fe(CN)_6^{3-}$ (right side) during charge and b) $Zn(OH)_4^{2-}$ (left side) and $Fe(CN)_6^{4-}$ (right side) during discharge.

Fig. 6 Charge and discharge voltage profiles of the battery with different electrode thicknesses.

Fig. 7 The species distribution of different electrode thickness at 50% stage: (a) $Zn(OH)_4^{2-}$ (left side) and $Fe(CN)_6^{3-}$ (right side) during charge and (b) $Zn(OH)_4^{2-}$ (left side) and $Fe(CN)_6^{4-}$ (right side) during discharge.

Fig. 8 Charge and discharge voltage profiles of the battery with different electrode porosity.

Fig. 9 The species distribution of different electrode porosity at 50% stage: (a) $Zn(OH)_4^{2-}$ (left side) and $Fe(CN)_6^{3-}$ (right side) during charge and (b) $Zn(OH)_4^{2-}$ (left side) and $Fe(CN)_6^{4-}$ (right side) during discharge.

Fig. 10 Performance comparison between the initial and optimized design. (a) Charge and discharge voltage profiles. (b-c) The species distribution at 50% stage: (b) $Zn(OH)_4^{2-}$ (left side) and $Fe(CN)_6^{3-}$ (right side) during charge and (c) $Zn(OH)_4^{2-}$ (left side) and $Fe(CN)_6^{4-}$ (right side) during discharge.

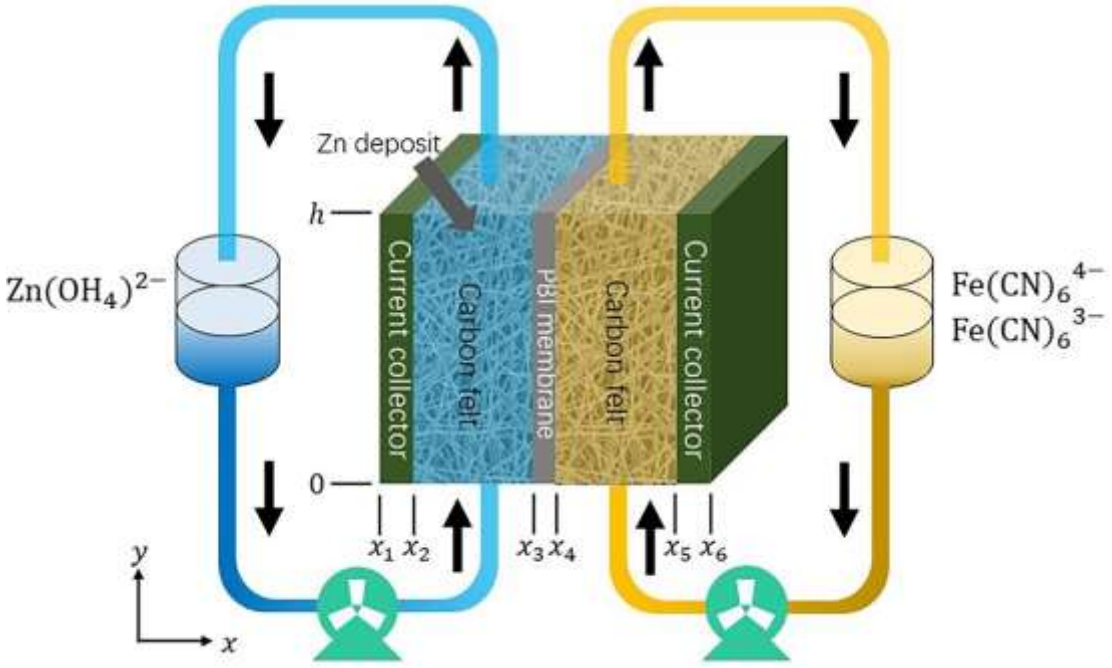

Fig. 1 Scheme of a zinc-iron flow battery. The computational domain is from 0 to x_6.

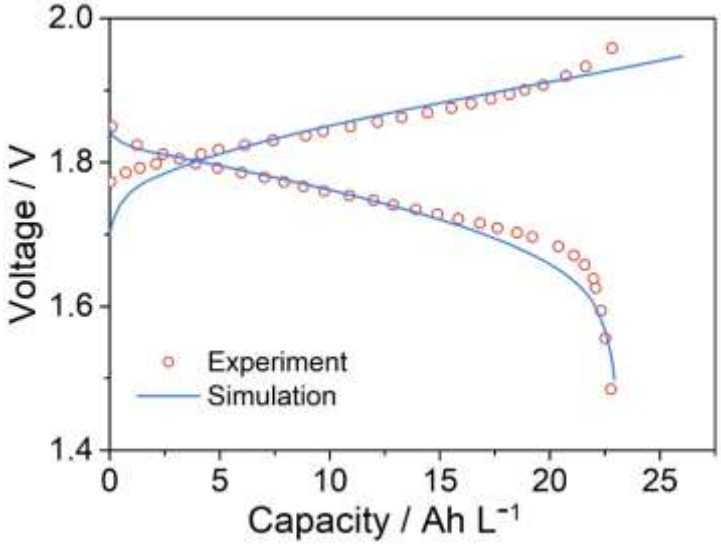

Fig. 2 Comparison of the simulated voltage profiles of a zinc-iron flow battery at the current density of 60 mA cm^{-2} with the experimental data.

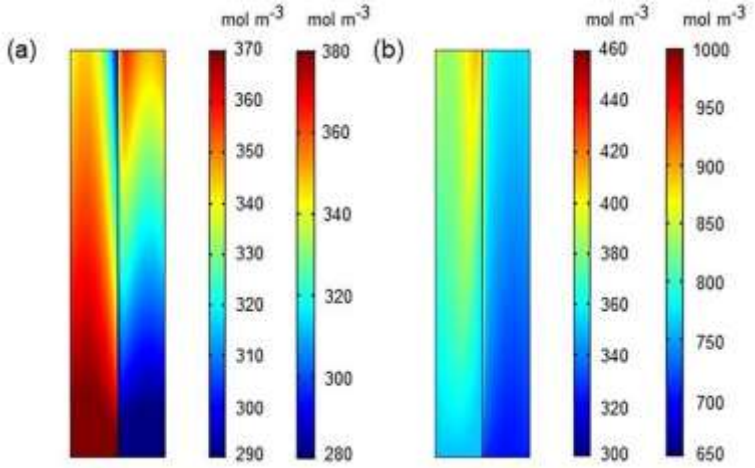

Fig. 3 The species distribution at 50% stage: (a) $Zn(OH)_4^{2-}$ (left side) and $Fe(CN)_6^{3-}$ (right side) during charge and (b) $Zn(OH)_4^{2-}$ (left side) and $Fe(CN)_6^{4-}$ (right side) during discharge.

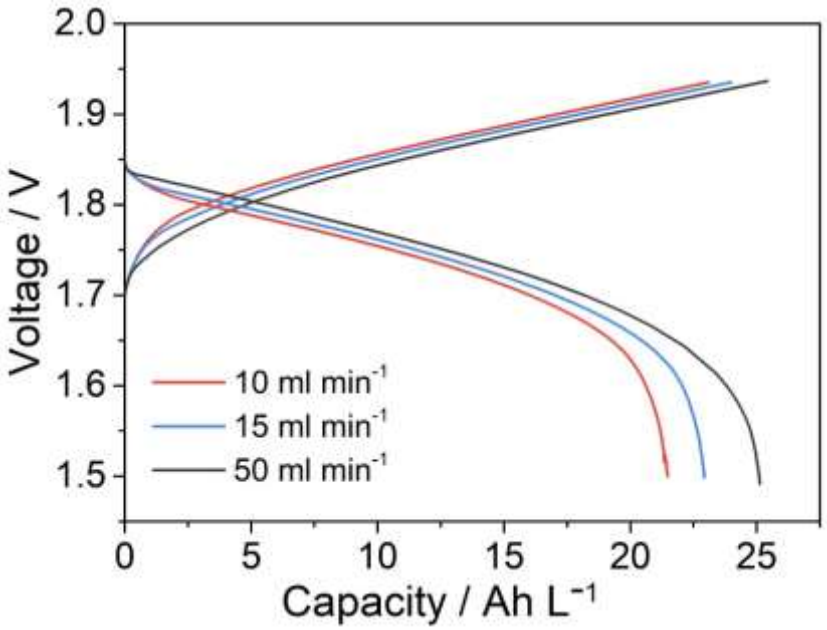

Fig. 4 Charge and discharge voltage profiles of the battery at different flow rates.

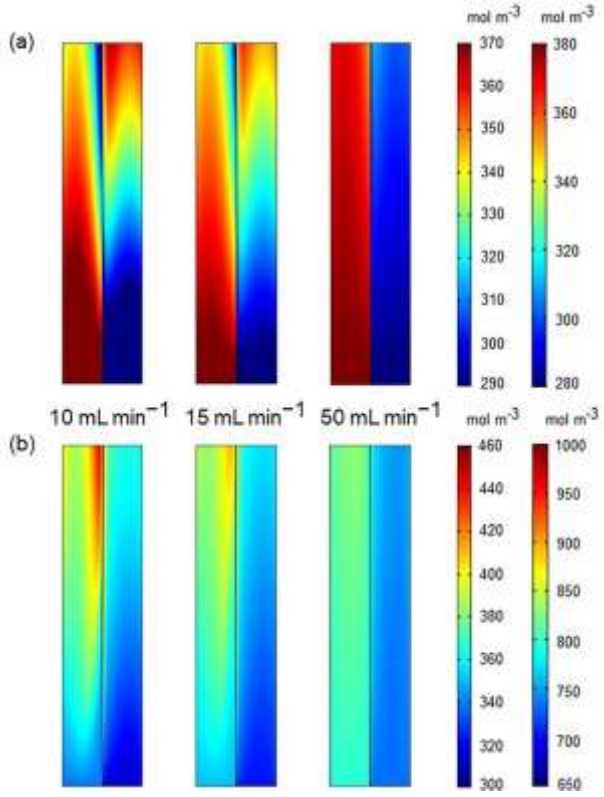

Fig. 5 The species distribution at different flow rates at 50% stage: (a) $Zn(OH)_4{}^{2-}$ (left side) and $Fe(CN)_6{}^{3-}$ (right side) during charge and b) $Zn(OH)_4{}^{2-}$ (left side) and $Fe(CN)_6{}^{4-}$ (right side) during discharge.

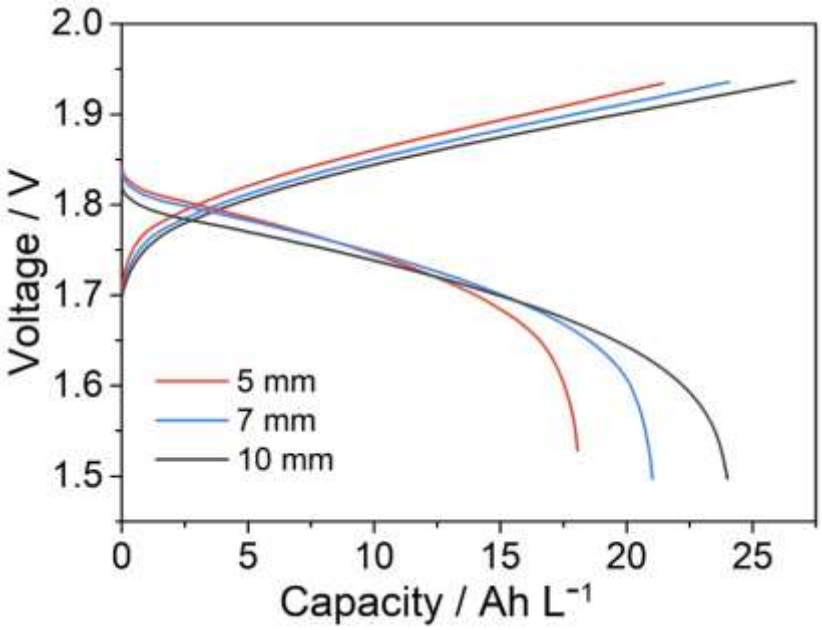

Fig. 6 Charge and discharge voltage profiles of the battery with different electrode thicknesses.

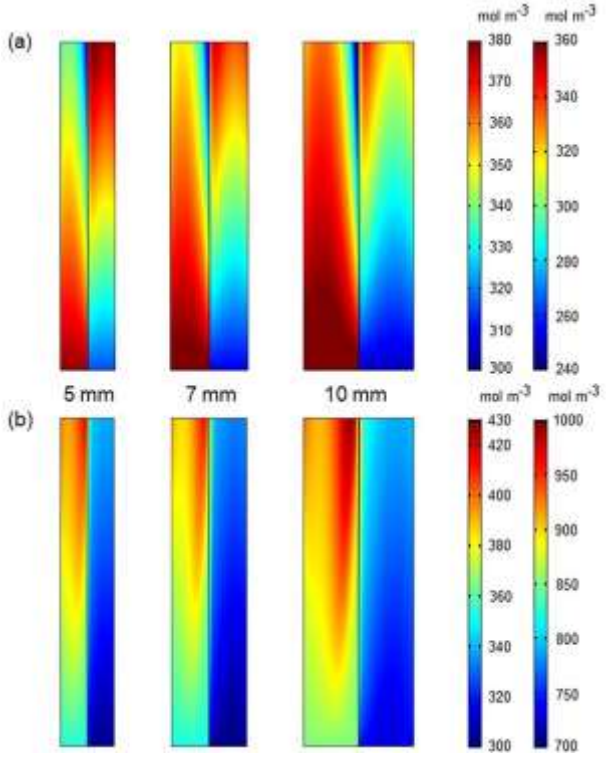

Fig. 7 The species distribution of different electrode thickness at 50% stage: (a) $Zn(OH)_4^{2-}$ (left side) and $Fe(CN)_6^{3-}$ (right side) during charge and (b) $Zn(OH)_4^{2-}$ (left side) and $Fe(CN)_6^{4-}$ (right side) during discharge.

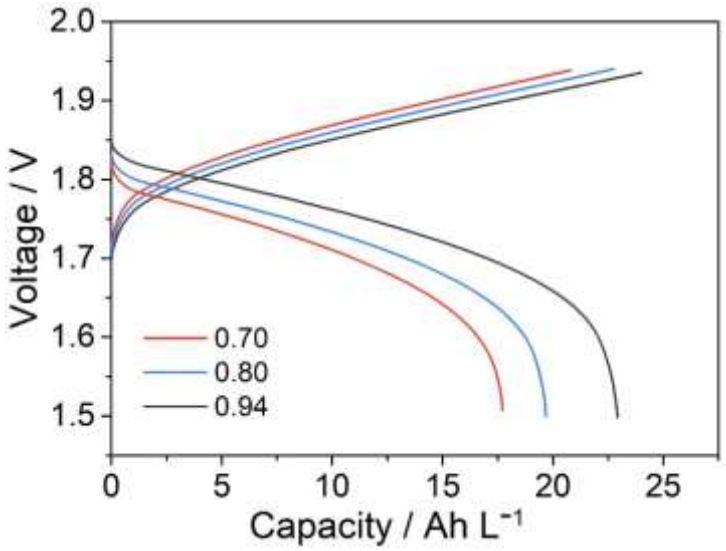

Fig. 8 Charge and discharge voltage profiles of the battery with different electrode porosity.

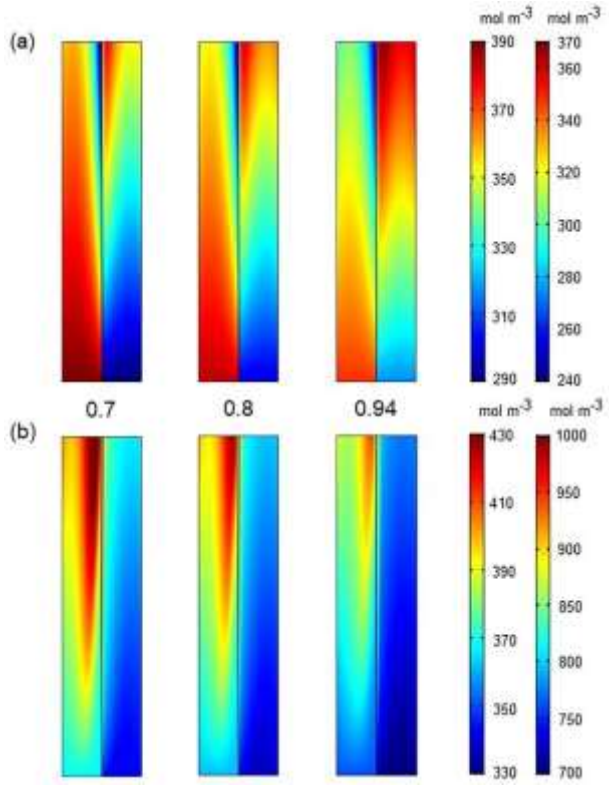

Fig. 9 The species distribution of different electrode porosity at 50% stage: (a) $Zn(OH)_4^{2-}$ (left side) and $Fe(CN)_6^{3-}$ (right side) during charge and (b) $Zn(OH)_4^{2-}$ (left side) and $Fe(CN)_6^{4-}$ (right side) during discharge.

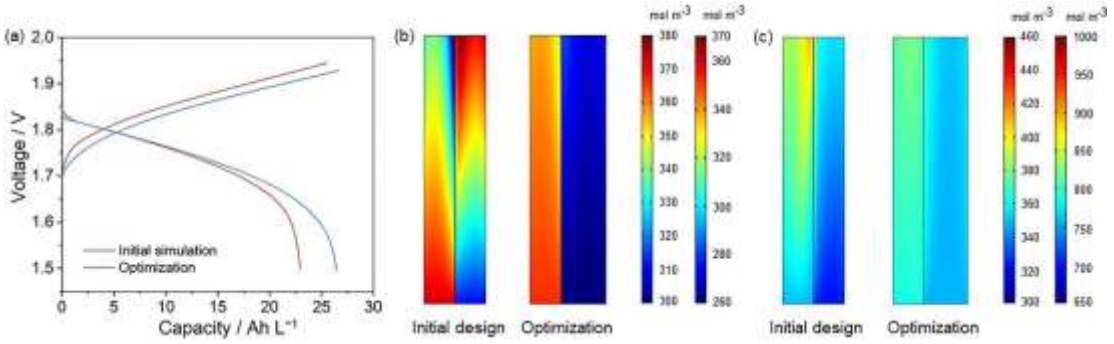

Fig. 10 Performance comparison between the initial and optimized design. (a) Charge and discharge voltage profiles. (b-c) The species distribution at 50% stage: (b) $Zn(OH)_4^{2-}$ (left side) and $Fe(CN)_6^{3-}$ (right side) during charge and (c) $Zn(OH)_4^{2-}$ (left side) and $Fe(CN)_6^{4-}$ (right side) during discharge.